

# Convective Schemes for Capturing Interfaces of Free-Surface Flows on Unstructured Grids

M. Darwish and F. Moukalled  
American University of Beirut,  
Faculty of Engineering & Architecture,  
Mechanical Engineering Dept.,  
P.O. Box 11-0236, Riad El Solh Street,  
Beirut 1107 2020, Lebanon  
Email: [darwish@aub.edu.lb](mailto:darwish@aub.edu.lb)

## Abstract

In this paper, the general methodology used in constructing interface capturing schemes is clarified and concisely described. Moreover, a new interface capturing scheme, denoted by STACS, based on a switching strategy is developed. The accuracy of the new scheme is compared to the well known CICSAM and HRIC schemes by solving the following test problems: advection of (i) a hollow square, (ii) a rotated hollow square, (iii) and a hollow circle in an oblique velocity field, and (iv) a slotted circle in a rotating flow field. Results, displayed in the form of interface contours for the various schemes, reveal deterioration in the accuracy of CICSAM and HRIC schemes with their performance approaching that of the UPWIND scheme as the Courant number increases. On the other hand, predictions obtained with the new STACS scheme are by far more accurate and less diffusive preserving interface sharpness and Boundedness at all Courant number values considered.

**Keywords:** Free-Surface, Advection Schemes, Finite Volume, Volume of Fluid, Multiphase Flow.

## Nomenclature

<b>B</b>	body force per unit volume.
Co	Courant number.
$\mathbf{d}_{PF}$	distance vector between points $P$ and $F$ .
$f(\theta)$	blending function that varies between 0 and 1.
n	total number of fluids.
P	pressure or main grid point.
$r^{(k)}$	volume fraction of $k^{\text{th}}$ fluid.
$\tilde{r}^{(k)}$	normalized value of $r^{(k)}$ .
$\mathbf{S}_f$	surface vector.
t	time.
$U_f$	interface velocity flux ( $\mathbf{v}_f \cdot \mathbf{S}_f$ ).
$\mathbf{u}$	velocity vector shared by all fluids.
u, v	velocity components in x and y direction.
V	cell volume.

## Greek Symbols

$\rho, \rho^{(k)}$	average and $k^{\text{th}}$ fluid density.
$\Gamma$	diffusion coefficient.
$\mu, \mu^{(k)}$	average and $k^{\text{th}}$ fluid dynamic viscosity.
$\tau$	shear stress tensor.
$\theta$	angle between interface and cell face.

$\Delta t$       time step.

$\Delta x, \Delta y$     mesh size in x and y directions for Cartesian grid.

### **Subscripts**

C          refers to upwind grid point or convection differencing.

D          refers to downwind grid point.

f          refers to control volume face.

P          refers to main grid point.

T          refers to temporal discretization.

U          refers to grid point upwind of C grid point.

## Introduction

The last two decades have witnessed a sustained research effort in the area of Computational Fluid Dynamics (CFD) that have led, among other developments, to: (i) increased numerical accuracy through the development of High Resolution Schemes [1,2,3,4,5], (ii) improved numerical robustness through the development of general velocity-pressure coupling algorithms for the simulation of incompressible and compressible flows in the subsonic, transonic, supersonic, and hypersonic regimes [6,7], (iii) greater model complexity through the development of multi-fluid flow algorithms [8,9], (iv) and higher efficiency through the development of more efficient solvers and robust multigrid acceleration techniques [10,11,12,13,14]. A major driver behind these developments have been the growing need in a number of industries (e.g. automotive, chemical processing, aeronautic, etc.) for a numerical simulation tool to help engineers and developers tackle problems of continuously increasing complexity. In specific, the expanding role of CFD as an engineering tool in ship design and metal casting [15,16] has put a renewed focus on the development of numerical techniques for the simulation of free-surface flows. The proper simulation of these types of flows requires a special set of numerical techniques to effectively handle a number of special flow features such as high density ratios (air, water), essential role of body-type forces (gravity, surface tension, etc. ), large pressure differences at fluid-fluid interfaces, and finally and as critically the advection of sharp fluid-fluid interfaces.

One convenient and powerful method for the simulation of such flows on fixed grids (i.e. Eulerian framework) is the volume of fluid (VOF) method [17], originally developed by Nichols and Hirt [18,19]. In this method a scalar field (volume of fluid

field, designated in this work by the  $r$  field) is introduced in the discretized governing equations to describe the volume fraction of a fluid filling a cell. The value of this  $r$  field is zero when the cell does not contain the  $r$  field associated fluid, and one when the cell is totally filled with that fluid. Cells located at the interface are filled with several fluids, thus the  $r$  fields at these locations have values between zero and one. The VOF method is capable of modeling flows with complex free surface geometries, including flows where fluid volumes separate and reattach; yet it is remarkably economical in computational terms, requiring only a mesh-sized array for storing the  $r$  field for a two-fluid model (or  $n-1$  mesh-sized arrays for an  $n$ -fluid model) and an algorithm to advect the  $r$  field(s) during each transient time step.

Because the  $r$  fields represent averaged volume fractions of fluids within each cell of the computational domain, information about interfaces is not readily available and as the fluids flow through the fixed grid, the fluid-fluid interfaces may cut through computational cells. In this case extreme care should to be taken in advecting the  $r$  fields so as to preserve the interface sharpness. For this to be realized, the discretization of the  $r$  equations in both the transient and spatial domains has to be accurate enough to prevent the smearing associated with numerical diffusion. The standard convective schemes are not suitable for advecting the  $r$  fields as they do not preserve the sharpness of the fluid-fluid interfaces.

For the spatial discretization, which is the focus of this paper, both High Resolution (HR) schemes and compressive schemes have been used to advect  $r$  fields, but these methods were found to be either too diffusive, not guaranteeing the sharp resolution of the multi-fluid interfaces essential in free surface flows, or overly compressive yielding a sharp but stepped and distorted interface [20]. Over the years, a number of advection schemes have been developed, which, for Eulerian meshes, can be

classified under two categories denoted in the literature by *Interface Tracking* methods and *Interface Capturing* methods. In *Interface Tracking* methods the interface is explicitly reconstructed and used in the evaluation of the advection scheme, i.e. the advected  $r$  fluxes depend explicitly on the position of the interface within the individual computational cell. Hence the accuracy of the reconstructed interface plays a critical role in the performance of the advection scheme. Examples of Interface tracking methods [21,22] include the well-known SLIC [23,24,25] and PLIC algorithms and their many variations (e.g. PROST [26], DDR [27], etc.). The main drawback of these methods is the algorithmic complexity involved in reconstructing the interface in a continuous manner across the computational domain, with this difficulty compounded in three-dimensional problems.

In *Interface Capturing* methods, the  $r$ -value at a control volume face can be formulated algebraically without reconstructing the interface [17,28,29,30, 31,32,33,34]. Generally in *Interface Capturing* methods a compressive scheme is used to avoid smearing of the interface. However, this has been found to lead to stepping of the interface (i.e. the loss of curvature), whenever the flow is not aligned with the computational grid. Workers have remedied this problem by adopting a switching strategy that toggles between a compressive and a non-compressive scheme depending on some criterion related to the  $r$  field. Many of these schemes base the switching criterion on a function of the angle formed between the interface normal direction, readily obtained using the gradient of the  $r$  field, and the grid orientation. Generally the base scheme is the upwind scheme but other higher order schemes could also be used.

For the discretization of the transient terms, which will be the focus of a future article, it suffices here to mention that the first order implicit Euler scheme, while

computationally robust and efficient, suffers from substantial numerical diffusion [35]. The second order Crank-Nicholson and the second order Euler schemes are better behaved in that respect but can still lead to over/under shoots with large time steps as they are not bounded. The standard second order Crank-Nicholson scheme is used in this work.

In this paper, the general methodology used in constructing interface capturing schemes is clarified and concisely described. Moreover, a new interface capturing scheme, denoted by STACS, based on a switching strategy is developed. The new scheme is compared, in terms of accuracy to the well known CICSAM [34] and HRIC [36] schemes by solving several test problems.

In the remainder of this article, after a brief description of the VOF method, the basic features of standard *Interface Capturing* schemes are introduced. This is followed by a discussion of the general strategy used for switching between compressive and HR schemes. Then, the HRIC and CICSAM schemes are reviewed and the new STACS scheme is presented. Finally, results related to the advection of three hollow shapes in an oblique velocity field [21,34,37], and a slotted circle in a rotational flow field [38] obtained using several schemes in addition to the newly developed STACS scheme at different Courant number values are presented and discussed.

## **The VOF method**

The VOF method, schematically depicted in Fig. 1, is a surface-capturing method for predicting flows composed of multiple immiscible fluids. The various fluids are assumed to share a common velocity field and solutions are obtained by solving the following averaged set of Navier-Stokes equations:

$$\begin{aligned} \frac{\partial(\rho)}{\partial t} + \nabla \cdot (\rho \mathbf{v}) &= 0 \\ \frac{\partial(\rho \mathbf{v})}{\partial t} + \nabla \cdot (\rho \mathbf{v} \mathbf{v}) &= \nabla \cdot \boldsymbol{\tau} - \nabla P + \mathbf{B} \end{aligned} \quad (1)$$

with density and viscosity evaluated using the following relations

$$\begin{aligned} \rho &= \sum_{k=1}^n r^{(k)} \rho^{(k)} \\ \mu &= \sum_{k=1}^n r^{(k)} \mu^{(k)} \end{aligned} \quad \text{where } n = \text{number of fluids} \quad (2)$$

where  $r^{(k)}$  represents the volume fraction of the  $k^{\text{th}}$  fluid. These  $r^{(k)}$  fields are computed by solving scalar convection equations defined as

$$\frac{\partial r^{(k)}}{\partial t} + \mathbf{v} \cdot \nabla r^{(k)} = 0 \quad \text{for } k = 1, 2, \dots, (n-1) \quad n = \text{number of fluids} \quad (3)$$

and constrained by a conservation of volume equation given by

$$\sum_{k=1}^n r^{(k)} = 1 \quad \text{for } k = 1, 2, \dots, n \quad n = \text{number of fluids} \quad (4)$$

For the case of incompressible fluids the continuity equation can be simplified to

$$\nabla \cdot \mathbf{v} = 0 \quad (5)$$

It is this form of the continuity equation (Eq. (5)) that is used in the derivation of the pressure correction equation in order to avoid numerical difficulties that arise when large disparities in fluid densities exist.

## Interface Capturing Schemes

From the previous section, it is obvious that the success of the VOF method depends heavily on the interface capturing scheme used in advecting the  $r$  field at a control volume face. The main difficulty associated with the development of such an advection scheme stems from the need to treat the discrete interface as an averaged scalar value over a computational cell. This weakness is illustrated, for example, by considering the advection of a rectangular fluid region over a time interval  $\Delta t$  with a

courant number of 0.5. The UPWIND scheme gives the solution shown in Fig. 2(a) while the exact solution is depicted in Fig. 2(b). The smearing of the profile is an outcome of treating the volume fraction as a standard scalar field rather than a representation of a fluid-fluid interface. A more appropriate treatment would be to use an interpolation profile for the  $r$  field that lumps the fluid near the interface in the manner shown in Fig. 2(b). This can be readily done with a downwind interpolation profile at the highlighted cell face.

Another difficulty is the well-known false diffusion problem of first order schemes, which deteriorate in accuracy when the flow is not oriented along a grid line (see Fig. 3). This drawback should preclude using the UPWIND scheme for capturing interfaces. Moreover, the DOWNWIND scheme being first order accurate, its performance is also highly dependent on the orientation of the flow relative to the grid. The effect in this case would be an over-compressed interface with no curvature (stepping effect). This artificial steepening of the  $r$  field was demonstrated by Leonard [39] through the advection of a one-dimensional semi-elliptic profile that was transformed into a step profile because of the use of a downwind-like advection scheme.

### **Blending Strategy for Interface-Capturing Schemes**

One way to address these two shortcomings is through a switching strategy that depends on the angle between the flow direction and the grid lines [29,40]. The best approach is to have a continuous switching function whereby the values of a Compressive and a High-Resolution advection scheme are blended together, with the blending factor depending on the angle between the flow direction and the grid lines. The angle can be determined using the grid orientation at the integration face and the gradient of the  $r$  field, whose unit vector represents the direction normal to the

interface (see Fig. 4). This general approach has been followed in the derivation of the new STACS scheme and is also utilized in the CICSAM [34] and the HRIC [36] schemes, even though different blending functions are used in these schemes, as will be described later.

From the above it is clear that an “interface Capturing” scheme based on the switching strategy should possess the following attributes:

- a. It should be based on a combination of Compressive and High-Resolution schemes.
- b. Its blending function should be based on the angle between the interface direction and the grid orientation, preferably in a continuous fashion.

### ***The Blending Function***

The reasoning followed in defining the blending function is illustrated in Fig. 5. If the cell has started to be filled with fluid from the upwind side of the interface and the interface is parallel to the cell face (Fig. 5(a)) then only fluid present at the downstream cell should be convected through the cell face. In this case a compressive scheme should be used. However if the interface is perpendicular to the cell face (Figure 5(b)) then the convected fluid is expected to be of the same composition as the upwind cell, in this case a HR scheme would be appropriate. When the fluid-fluid interface is parallel to the cell face but most of the cell is filled with fluid from the upwind side of the interface (Figure 5(c)), then either scheme could be used. The above mentioned situations represent extreme cases in which the fluid-fluid interface is either parallel or perpendicular to the control volume face. In general, the angle between the interface and cell face is between these two extremes (i.e. the angle  $\theta$  usually varies between 0 and 90, Figure 5(d)) and the value of  $r$  at the interface should

be obtained by blending the advection schemes of the extreme cases, with the blending function given as

$$\tilde{r}_f = \tilde{r}_{f(\theta)} = \tilde{r}_{f(Compressive)} f(\theta_f) + \tilde{r}_{f(HR)} [1 - f(\theta_f)] \quad (6)$$

where  $f(\theta_f)$  is a function that varies between 0 and 1 and  $\tilde{r}$  is the normalized value of  $r$  defined as

$$\tilde{r} = \frac{r - r_U}{r_D - r_U} \quad (7)$$

with the subscripts U and D referring to values at the upstream and downstream locations as shown in Fig. 2.

### **HRIC Scheme**

The High Resolution Interface Capturing scheme (HRIC) of Muzaferija [36,41] is based on a blending of the Bounded Downwind (BD) and Upwind Differencing schemes (UD), with the aim of combining the compressive property of the BD scheme, which can be viewed as a steady-state version of the Hyper-C scheme [39], with the stability of the UD scheme. The normalized functional relationship of the BD scheme, whose Normalized Variable Diagram is displayed in Fig. 6, is given by

$$\tilde{r}_{f(BD)} = \begin{cases} 2\tilde{r}_C & 0 < \tilde{r}_C \leq 0.5 \\ 1 & 0.5 < \tilde{r}_C \leq 1 \\ \tilde{r}_C & otherwise \end{cases} \quad (8)$$

The functional relationship of the HRIC scheme is also function of the angle  $\theta$  between the normal to the interface (defined by the gradient of the  $r$  field) and the normal to the cell face [41]. For an interface aligned with the cell face ( $\theta=0$ ) the bounded downwind scheme is used, while for an interface perpendicular to the cell face the upwind scheme is used. For an interface with  $\theta$  between these two limits,

$f(\theta_f)$  is chosen to be  $\sqrt{\cos(\theta_f)}$  and the blending formula is given by

$$\tilde{r}_{f(\theta)} = \tilde{r}_{f(BD)}\sqrt{\cos(\theta_f)} + \tilde{r}_{f(UPWIND)}\left(-\sqrt{\cos(\theta_f)}\right) \quad (9)$$

With this formulation (Eq. (9)), the blending of the UPWIND and DOWNWIND schemes is dynamic and accounts for the local distribution of the  $r$  field. Muzaferija further modifies the value of  $\tilde{r}_f$  to account for the local Courant number (Co) defined by

$$Co_f = \frac{\mathbf{v}_f \cdot \mathbf{S}_f \Delta t}{V_f} \quad (10)$$

For Courant number below 0.3 the scheme is not modified (*i.e.*  $\tilde{r}_f = \tilde{r}_{f(\theta)}$ ), while for a courant number above 0.7 the upwind scheme is used. For Co values between 0.3 and 0.7, the interface value computed from Eq. (9) is blended with the upwind scheme to yield the final  $r$  value at the fluid-fluid interface, which in normalized form is written as

$$\tilde{r}_f = \tilde{r}_{f(\theta)} + \left(\tilde{r}_{f(UPWIND)} - \tilde{r}_{f(\theta)}\right) \frac{0.7 - Co_f}{0.7 - 0.3} \quad (11)$$

The Normalized Variable Diagrams of the HRIC scheme for Co values in the various regimes are depicted in Fig. 7. It is clear from the NVD diagram that for courant number values above 0.7 the HRIC scheme basically reverts to the very diffusive UPWIND scheme, and even for moderate values of the Courant number, the scheme would still be very diffusive.

### **CICSAM Scheme**

The CISCAM scheme of Ubbink [34] is also an interface capturing scheme based on the blending strategy. However rather than choosing the DOWNWIND and UPWIND schemes as base schemes, it uses, respectively, the HYPER-C scheme [42] and the ULTIMATE-QUICKEST scheme of Leonard [43], with HYPER-C being utilized when the cell face is perpendicular to the interface normal vector and the

ULTIMATE-QUICKEST (UQ) employed when the normal vector to the face is aligned with the normal to the interface. The HYPER-C scheme is a bounded downwind scheme that is constructed by enforcing the transient CBC criterion onto the DOWNWIND scheme and is expressed as

$$\tilde{r}_{f(HYPER-C)} = \begin{cases} \min\left(1, \frac{\tilde{r}_C}{Co}\right) & 0 \leq \tilde{r}_C \leq 1 \\ \tilde{r}_C & otherwise \end{cases} \quad (12)$$

Moreover, the normalized functional relationship of the UQ scheme is given by

$$\begin{aligned} \tilde{r}_{f(UQ)} &= Co\{\tilde{r}_{f(UPWIND)}\} + (1-Co)\{\tilde{r}_{f(QUICK)}\} \\ where \\ \tilde{r}_{f(QUICK)} &= \frac{3}{8} + \frac{3}{4}\tilde{r}_C \\ \tilde{r}_{f(UPWIND)} &= \tilde{r}_C \end{aligned} \quad (13)$$

Furthermore, the CICSAM scheme can mathematically be written as

$$\tilde{r}_{f(CICSAM)} = \tilde{r}_{f(HYPER-C)}f(\theta_f) + \tilde{r}_{f(UQ)}[1 - f(\theta_f)] \quad (14)$$

The blending function  $f(\theta_f)$  is based on the angle  $\theta_f$  between the gradient of the volume fraction at the interface and the normal to the cell face (see Fig. 4). The equations for the angle and blending function are computed from

$$\theta_f = \arccos \left| \frac{\nabla r_f \cdot \mathbf{d}_{PF}}{\|\nabla r_f\| \|\mathbf{d}_{PF}\|} \right| \quad (15)$$

and

$$f(\theta_f) = \min\left(\frac{\cos(2\theta_f) + 1}{2}, 1\right) \quad (16)$$

For an angle  $\theta_f=90^\circ$ , i.e. when the interface normal is perpendicular to the cell face normal,  $f(\theta_f)$  is zero and the UQ scheme is used, and for  $\theta_f=0$ , i.e. when the flow interface is aligned with the face normal, the HYPER-C scheme is used. The NVD of

the CICSAM scheme, depicted in Fig. 8, reveals that with increasing courant number the scheme becomes more and more diffusive as its NVF function reverts to the UPWIND scheme.

### ***STACS Scheme***

As will be shown in the results section, predictions generated using the above schemes deteriorate with increasing values of the courant number as these schemes blend with the upwind scheme and become identical to it at a courant number of 0.7 for HRIC and 1 for CICSAM. The authors of this article have found this behavior to be a result of the used temporal bounding, originally designed by Leonard [39] for the *explicit* QUICKEST scheme. While this is needed for explicit transient schemes, its use in an implicit method increases numerical diffusion as explained below.

Jasak [44] has shown that numerical diffusion from convection differencing schemes can be written as

$$\nabla \cdot (\Gamma_C \nabla r) \quad \text{with} \quad \Gamma_C = \frac{1}{2} \rho_f |U_f| |d| \quad \text{for the UPWIND scheme} \quad (17)$$

while numerical diffusion from temporal discretization is given by

$$\nabla \cdot (\Gamma_T \nabla r) \quad \text{with} \quad \begin{cases} (\Gamma_T)_{max} = \frac{1}{2} (Co) \rho_f |U_f| |d| & \text{for the implicit Euler scheme} \\ (\Gamma_T)_{max} = -\frac{1}{2} (Co) \rho_f |U_f| |d| & \text{for the explicit Euler scheme} \end{cases} \quad (18)$$

It is clear that the numerical anti-diffusion (negative diffusion) resulting from the explicit Euler scheme cancels the numerical diffusion of the upwind scheme at Courant number of 1. Therefore the use of the upwind scheme as the courant number approaches 1 is actually desirable with the explicit Euler scheme. On the other hand the numerical diffusion of the Implicit Euler scheme adds (rather than cancels) to that resulting from the UPWIND scheme with the total numerical diffusion increasing

with the Courant number and yielding excessively diffusive profiles. This clearly explains the deterioration in performance experienced by the HRIC and CICSAM schemes with increasing Courant number.

The deficiencies associated with the above schemes have motivated the development of a new interface capturing scheme based on the aforementioned strategy but that overcomes the outlined shortcomings. In the newly suggested Switching Technique for Advection and Capturing of Surfaces scheme (STACS), the selected compressive scheme is SUPERBEE [42], a bounded version of the downwind scheme, while the High-Resolution scheme is STOIC [45]. Moreover, because of the use of an implicit transient discretization, no transient bounding is applied. Furthermore in order to minimize the stepping behavior of the highly compressive SUPERBEE scheme, the blending between the two schemes is performed using equation (6) with  $f(\theta_f)$  set to  $[\cos(\theta_f)]^4$  that enables a rapid but smooth switching away from the Compressive scheme for the case where the normal to the free surface face is not along the grid direction. The normalized variable diagrams of the SUPERBEE, STOIC and STACS schemes are displayed in Figs. 9(a), 9(b), and 9(c) respectively.

The normalized variables relationship for the STACS scheme is given by

$$\tilde{r}_{f,STACS} = \tilde{r}_{f,SUPERBEE} \cos(\theta)^4 + \tilde{r}_{f,STOIC} (1 - \cos(\theta))^4 \quad (19)$$

where  $\tilde{r}_{f,SUPERBEE}$  and  $\tilde{r}_{f,STOIC}$  are obtained from

$$\tilde{r}_{f,SUPERBEE} = \begin{cases} \tilde{r}_C & \tilde{r}_C \leq 0 \\ 1 & 0 < \tilde{r}_C < 1 \\ \tilde{r}_C & 1 \leq \tilde{r}_C \end{cases} \quad \tilde{r}_{f,STOIC} = \begin{cases} \tilde{r}_C & \tilde{r}_C \leq 0 \\ \frac{1}{2} + \frac{1}{2}\tilde{r}_C & 0 < \tilde{r}_C \leq \frac{1}{2} \\ \frac{3}{8} + \frac{3}{4}\tilde{r}_C & \frac{1}{2} < \tilde{r}_C \leq \frac{5}{6} \\ 1 & \frac{5}{6} < \tilde{r}_C \leq 1 \\ \tilde{r}_C & 1 < \tilde{r}_C \end{cases} \quad (20)$$

This strategy is not limited to the above schemes rather it can be used to devise a family of free-surface advection schemes by using different combination of Compressive/HR schemes (e.g. SMART [43], OSHER [46], etc...).

## Results and Discussion

This section presents four test cases comparing the performance of the CICSAM, HRIC, and the new STACS interface capturing schemes in addition to the well-known UPWIND and SMART schemes over structured and unstructured grid systems. Results generated are reported in the form of  $r$ -contour plots for three values of the Courant number. In all figures, contours are displayed for  $0.05 \leq r \leq 0.95$  with a step size  $\Delta r = 0.06923$ . All residuals are normalized by their respective local fluxes and at any time step computations are terminated when the maximum normalized residual drops below a very small number  $\epsilon_s$ , which is set to  $10^{-6}$ . Moreover, all calculations are performed assuming that the densities of the fluid and convected shape are equal and surface tension effects are negligible. The exact solutions for the problems considered are presented in Fig. 10.

### Advection of Hollow Shapes in an Oblique Velocity Field

Three different hollow shapes [47,37] are convected in an oblique velocity field defined by  $\mathbf{v}[2,1]$ . The computational domain is a square of side 1m, subdivided into  $200 \times 200$  (40,000) square control volumes for structured grid computations and 47,240 triangular elements for unstructured grid calculations. The following three shapes, depicted in Figs. 10(a), 10(b), and 10(c), are considered:

1. A hollow square (Fig. 10(a)) aligned with the co-ordinate axes of an outer side length 0.2m and inner side length 0.1m, which for the structured mesh used are subdivided into 40 and 20 cells respectively.

2. A hollow square rotated through an angle of  $26.57^\circ$  with respect to the x-axis (Fig. 10(b)) of dimensions similar to those of the above hollow square.
3. A hollow circle (Fig. 10(c)) with an outer diameter of length 0.2m and inner diameter of 0.1 m spanning 40 and 20 structured cells respectively.

All shapes are initially centered at (0.2, 0.2) m with their exact positions centered at (0.8, 0.5) m after 0.3 s, as displayed in Figs. 10(a)-10(c). Computations, using the second order Crank-Nicholson scheme, are performed for three different time steps  $\Delta t = 0.0004167$ ,  $0.0008333$ , and  $0.0012498$  s yielding, over the structured grids, a Courant number of value 0.25, 0.5, and 0.75 respectively. Since it is hard to control the Courant number over the unstructured grid, these values are denoted by low, medium, and high on the presented results. The Courant number is defined as

$$Co = \sum_{\sim f(P)} \frac{\|(\mathbf{v}_P \cdot \mathbf{S}_f), 0\| \Delta t}{V_P} \quad (21)$$

which for Cartesian grid recovers its standard multi-dimensional form given by

$$Co = \frac{u \Delta t}{\Delta x} + \frac{v \Delta t}{\Delta y} \quad (22)$$

Contour plot results of the  $r$  fields for the various shapes and schemes at different  $Co$  values after the lapse of 0.3 s are presented in Figs. 11-16. As depicted, the trend is the same for all shapes. The UPWIND scheme profiles (Figs. 11(a)-16(a)) are highly diffusive at all  $Co$  considered. The Smart scheme produces results that are better than those obtained with the upwind scheme however it does not resolve sharply the interfaces (Figs. 11(b)-16(b)). The  $Co$  seems to have little effect on the convected shapes predicted by both schemes with the maximum value of  $r$  slightly varying. On the other hand, results generated by the CICSAM (Figs. 11(c)-16(c)) and HRIC (Figs. 11(d)-16(d)) schemes show high dependence on  $Co$  with the predicted shapes

becoming increasingly diffusive with increasing values of  $Co$ . As expected, the maximum predicted value of  $r$  decreases as  $Co$  increases since the schemes approach the UPWIND scheme. The HRIC and CICSAM schemes revert to the UPWIND scheme at  $Co \geq 0.7$  and 1, respectively. This explains the analogous shapes obtained by the HRIC and UPWIND schemes at  $Co=0.75$ . The best profiles are the ones obtained by the newly developed STACS scheme (Figs. 11(e)-16(e)), which are almost independent of  $Co$  with a maximum  $r$  value of 1 and preserving the sharpness of the interfaces. The better performance of STACS in comparison with other schemes is due to the reasons explained in the previous section.

By comparing contours obtained over structured (Figs. 11, 13, and 15) and unstructured meshes (Figs. 12, 14, and 16), it is clear that results follow similar trends with the quality of those obtained on structured rectangular grids being slightly better. The small wiggles that are mildly polluting some of the unstructured grid results are due to larger variations in the blending angle  $\theta$  as compared to the structured grid case. This is in addition to a higher  $Co$  value due to the larger number of triangular elements. Nevertheless the performance of STACS is by far more superior to all other schemes.

### **Advection of a Slotted Circle in a Rotational Flow Field**

The solid-body rotation of an object poses a test problem with a trivial exact solution [47,38,48]. However it is a tough problem with regard to advection schemes. The test in question involves the rotation of a slotted circle around an external point. The computational domain, schematically depicted along with the exact solution in Fig. 10(d), is a square of dimensions [4, 4] m discretized into 200x200 (40,000) square control volumes for structured grid computations giving a step size of  $\Delta x = \Delta y = 5 \times 10^{-3}$

and 65,536 triangular elements for unstructured grid calculations. The circle of diameter 1 m (occupying 50 structured cells) has its centre at (2,2.65) m and is cut by a slot of width 0.12 m (occupying 6 structured cells). The rotation of the slotted circle is driven by a vortex flow centered at the middle of the domain (2,2) of angular velocity  $\omega=0.5$  rad/s. The time required by the slotted circle to complete a revolution is  $2\pi/\omega$  s. With the geometry considered, the Courant number varies from a minimum (equals to  $0.15*\omega*\Delta t/\Delta x$ ) at point (2, 2.15) to a maximum (equals to  $1.15*\omega*\Delta t/\Delta x$ ) at (2, 2.65). The problem is solved for three different local Courant number values such that the total period required for a revolution is subdivided into 1262, 841, and 421 time steps, respectively.

As for the previous tests, predictions generated by the various schemes over structured and unstructured grids are presented in the form of contour plots for the  $r$  field in Figs. 17 and 18, respectively. The trend of results generated by the UPWIND (Figs. 17(a) and 18(a)), SMART (Fig. 17(b) and 18(b)), and STACS (Fig. 17(e) and 18(e)) is the same as for the previous test cases. Profiles generated by CICSAM (Fig. 17(c) and 18(c)) and HRIC (Fig. 17(d) and 18(d)) may look different than the ones generated earlier but are essentially similar as will be clarified. For these two schemes, contours are more diffusive on the upper side. This is due to the variation in the Courant number, which is higher on the upper side than on the lower side. Unlike the previous test cases for which the  $Co$  was constant, in this problem it increases with distance from the center of rotation. As the local value of  $Co$  increases, the contribution of the upwind value to the scheme increases resulting in the displayed profiles. Other schemes do not seem to be affected by the Courant number as their functional relationships are not affected by its value. Again structured grid results (Fig. 17) are more accurate than unstructured grid predictions (Fig. 18) due to a higher

Courant number resulting from the larger number of triangular elements used. The best performance however remains for STACS, which is capable of resolving all interfaces accurately and at all  $Co$  considered.

### **Closing Remarks**

A general methodology for constructing interface capturing schemes based on a switching strategy was presented. The method was used to develop a new interface capturing scheme denoted by STACS. The accuracy of the newly developed scheme on structured and unstructured grid networks was compared against the UPWIND, SMART, CICSAM, and HRIC schemes by solving several pure advection problems and was shown to be by far more accurate preserving sharpness of interfaces. Unlike the HRIC and CICSAM schemes, STACS's performance was shown to be independent, for all cases considered, of the Courant number value.

## Figure Captions

- Fig. 1 Schematic of the Volume of Fluid (VOF) Method.
- Fig. 2 Advection of a fluid block at a Courant number of value 0.5 using (a) the upwind scheme and (b) the exact solution.
- Fig. 3 Final shape of an initially round droplet after advection in four directions using the VOF with a standard compressive scheme.
- Fig. 4 Angle between interface and cell face.
- Fig. 5 Blending Strategy for Interface Capturing Schemes.
- Fig. 6 The Normalized Variable Diagram (NVD) of the Bounded Downwind Scheme.
- Fig. 7 The Normalized Variable Diagram (NVD) of the HRIC scheme.
- Fig. 8 The Normalized Variable Diagram (NVD) of the CICSAM scheme.
- Fig. 9 The Normalized Variable Diagrams (NVD) of the (a) SUPERBEE, (b) STOIC, and (c) STACS scheme.
- Fig. 10 Schematics of the advected (a) hollow square, (b) rotated hollow square, (c) hollow circle, and (d) slotted circle problems.
- Fig. 11  $r$ -contour plots for the advection in an oblique flow field of the hollow square problem over a structured grid.

- Fig. 12  $r$ -contour plots for the advection in an oblique flow field of the hollow square problem over an unstructured grid.
- Fig. 13  $r$ -contour plots for the advection in an oblique flow field of the rotated hollow square problem over a structured grid.
- Fig. 14  $r$ -contour plots for the advection in an oblique flow field of the rotated hollow square problem over an unstructured grid.
- Fig. 15  $r$ -contour plots for the advection in an oblique flow field of the hollow circle problem over a structured grid.
- Fig. 16  $r$ -contour plots for the advection in an oblique flow field of the hollow circle problem over an unstructured grid.
- Fig. 17  $r$ -contour plots for the advection in a rotational flow field of the slotted circle problem over a structured grid.
- Fig. 18  $r$ -contour plots for the advection in a rotational flow field of the slotted circle problem over an unstructured grid.

## Figures

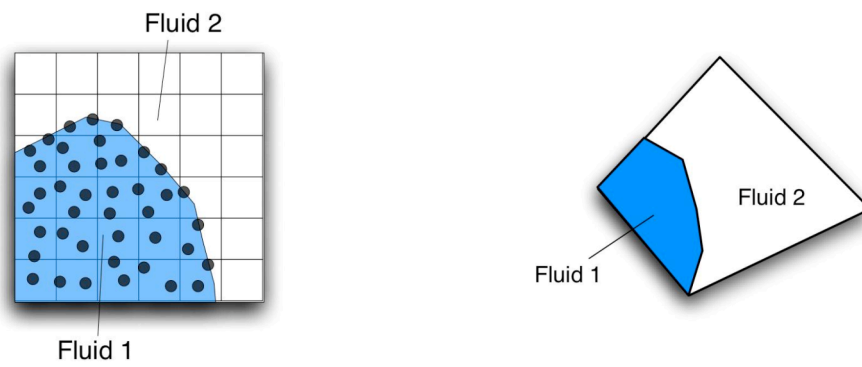


Fig. 1 Schematic of the Volume of Fluid (VOF) Method.

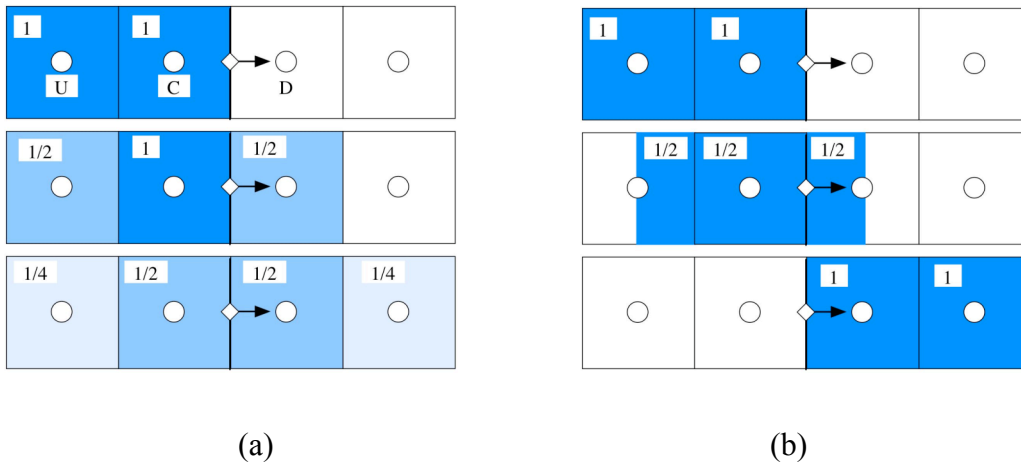


Fig. 2 Advection of a fluid block at a Courant number of value 0.5 using (a) the upwind scheme and (b) the exact solution.

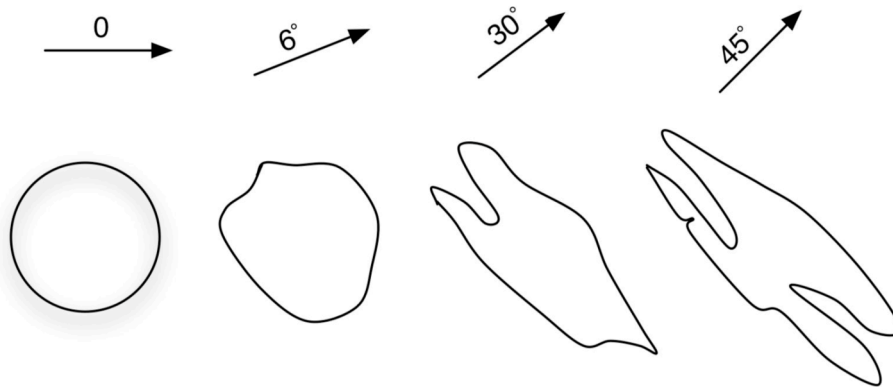


Fig. 3 Illustration of the shape of an initially round droplet after advection in four directions using the VOF with a standard compressive scheme.

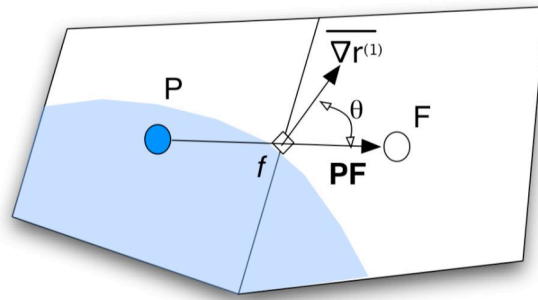
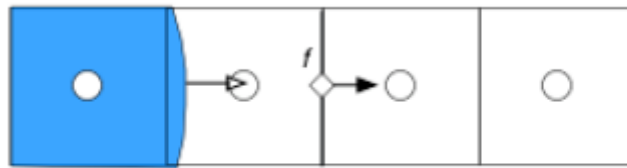
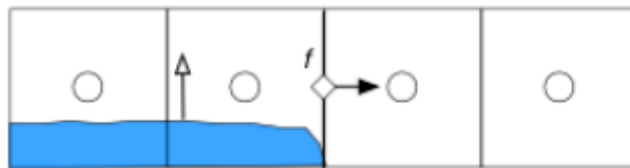


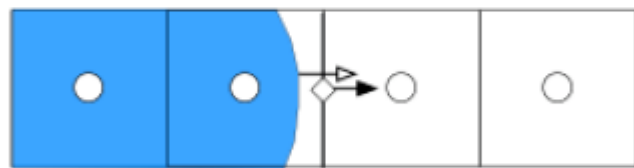
Fig. 4 Angle between interface and cell face.



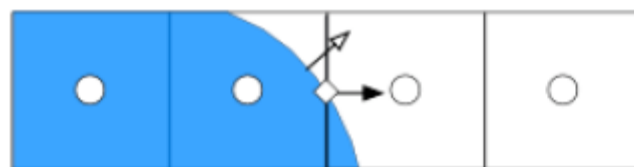
(a)



(b)



(c)



(d)

Fig. 5 Blending Strategy for Interface Capturing Schemes.

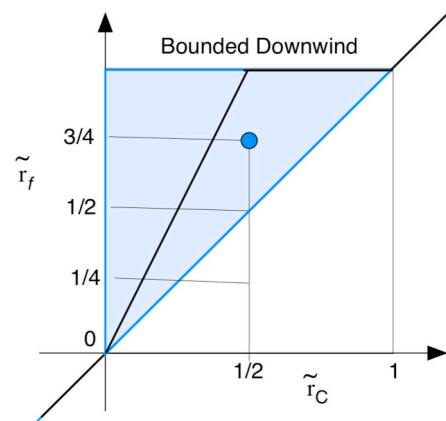


Fig. 6 The Normalized Variable Diagram (NVD) of the Bounded Downwind Scheme.

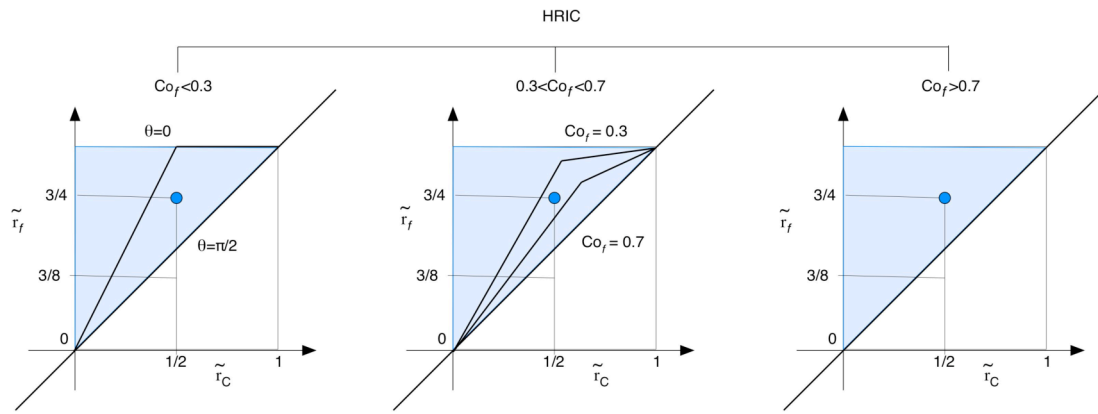


Fig. 7 The Normalized Variable Diagram (NVD) of the HRIC scheme.

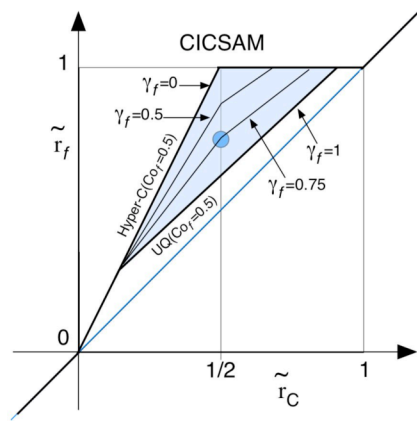


Fig. 8 The Normalized Variable Diagram (NVD) of the CICSAM scheme.

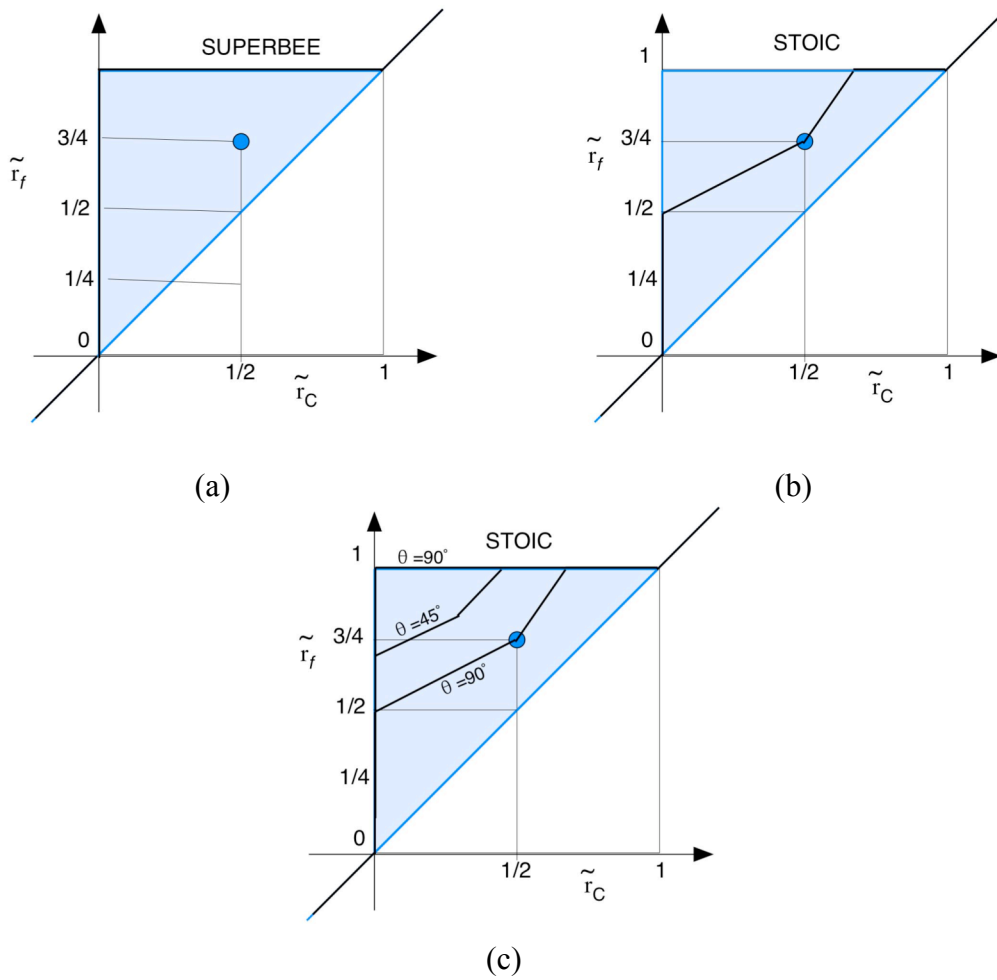
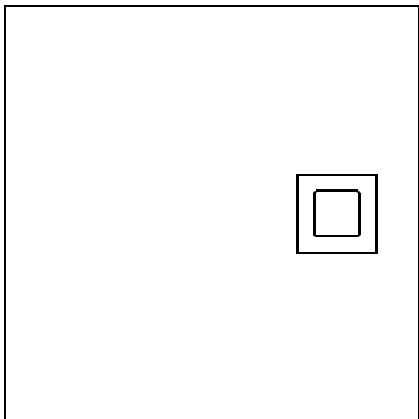
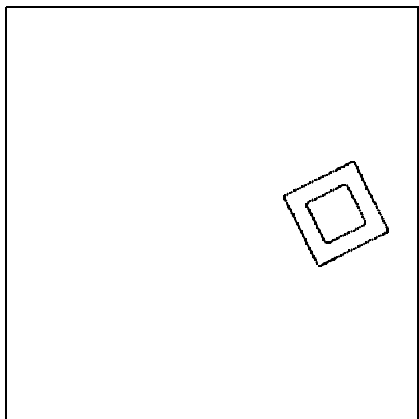


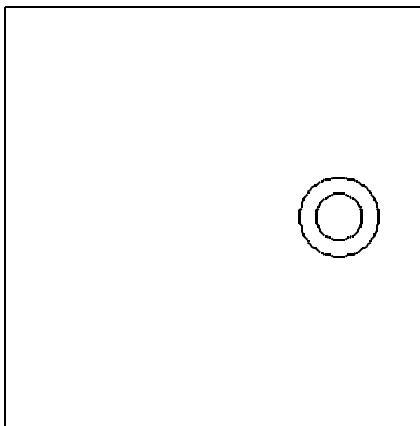
Fig. 9 The Normalized Variable Diagrams (NVD) of the (a) SUPERBEE, (b) STOIC, and (c) STACS scheme.



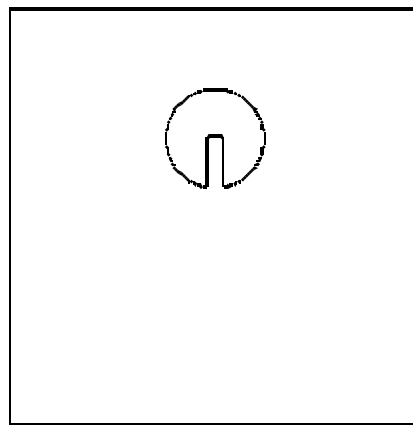
(a)



(b)



(c)



(d)

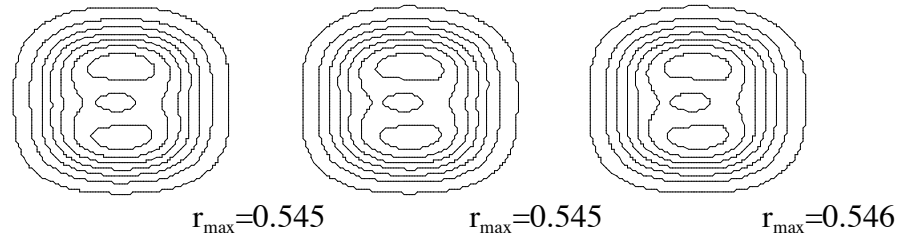
Fig. 10 Schematics of the advected (a) hollow square, (b) rotated hollow square, (c) hollow circle, and (d) slotted circle problems.

low Co

medium Co

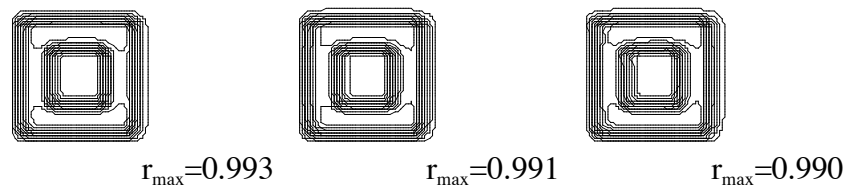
high Co

UPWIND



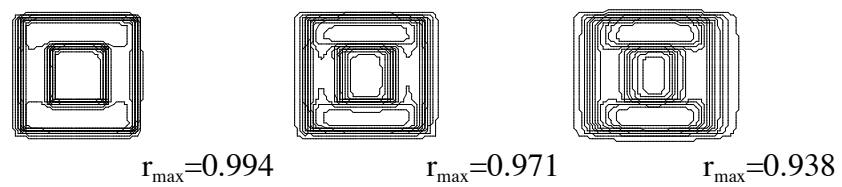
(a)

SMART



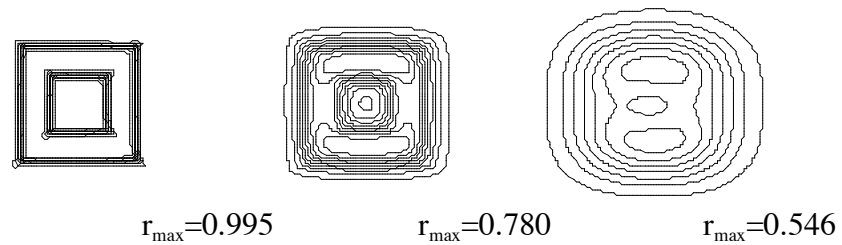
(b)

CICSAM



(c)

HRIC



(d)

STACS

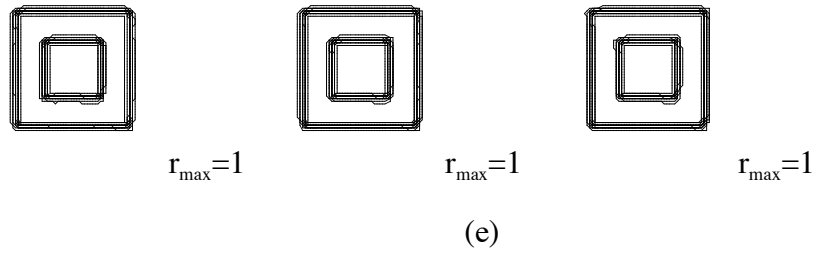
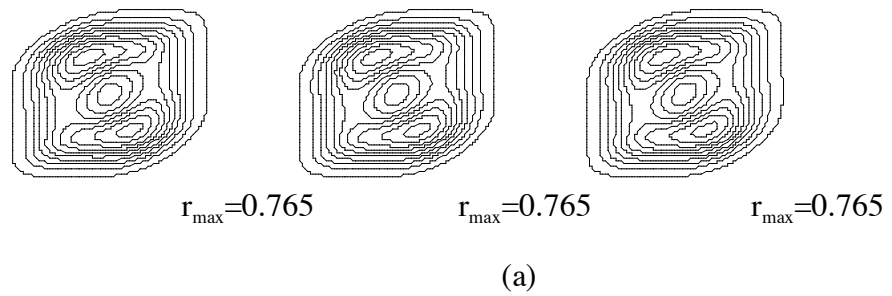


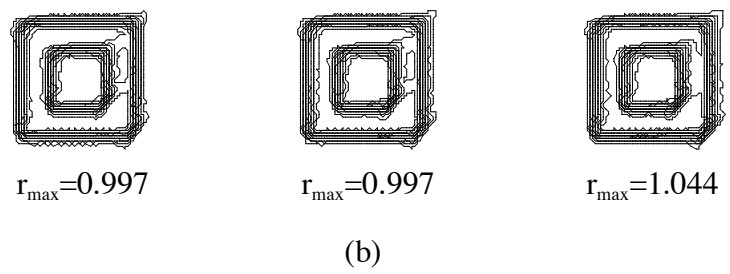
Fig. 11  $r$ -contour plots for the advection in an oblique flow field of the hollow square problem over a structured grid.

low Co                      medium Co                      high Co

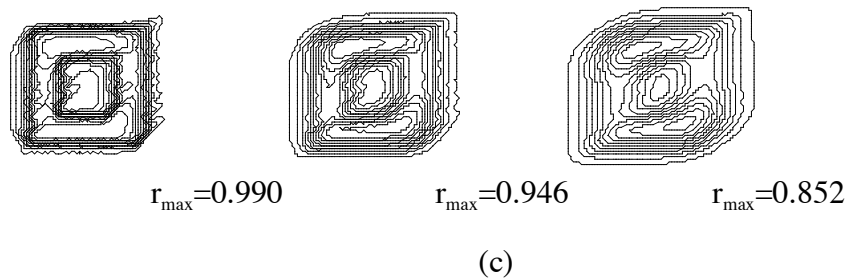
UPWIND



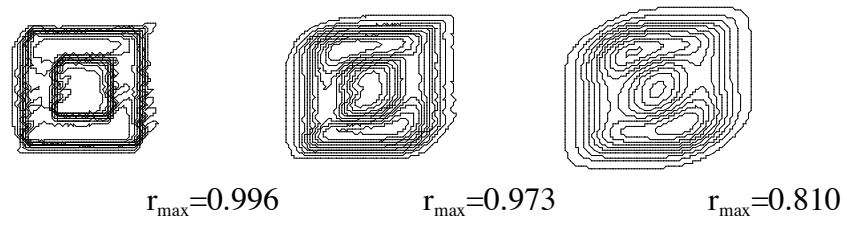
SMART



CICSAM

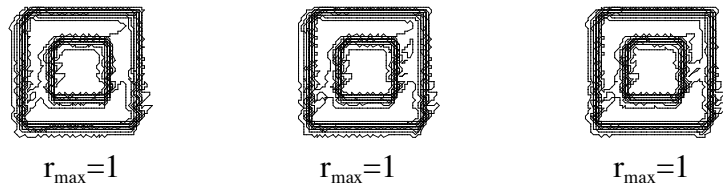


HRIC



(d)

STACS



(e)

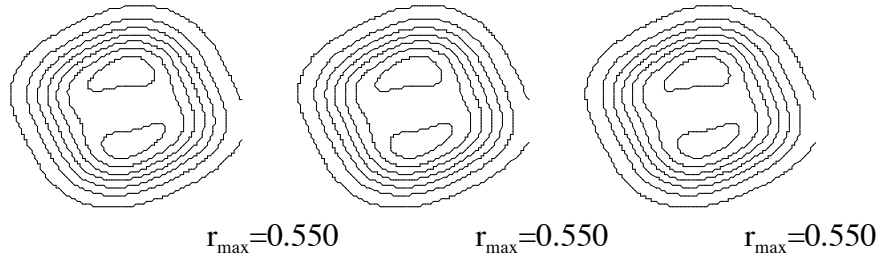
Fig. 12  $r$ -contour plots for the advection in an oblique flow field of the hollow square problem over an unstructured grid.

low Co

medium Co

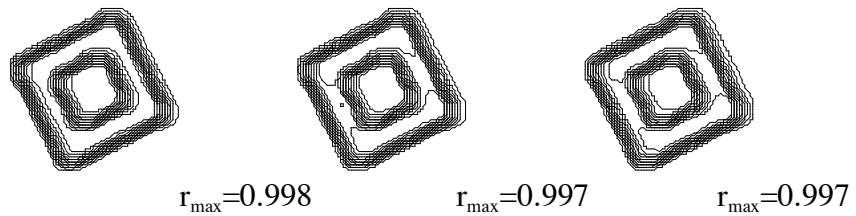
high Co

UPWIND



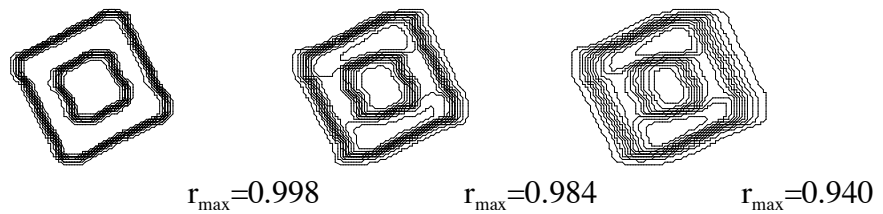
(a)

SMART



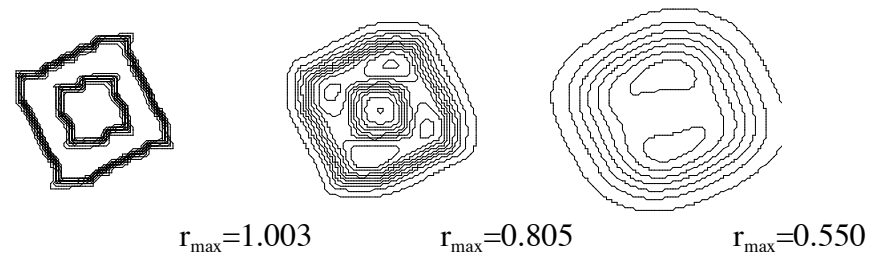
(b)

CICSAM



(c)

HRIC



(d)

STACS

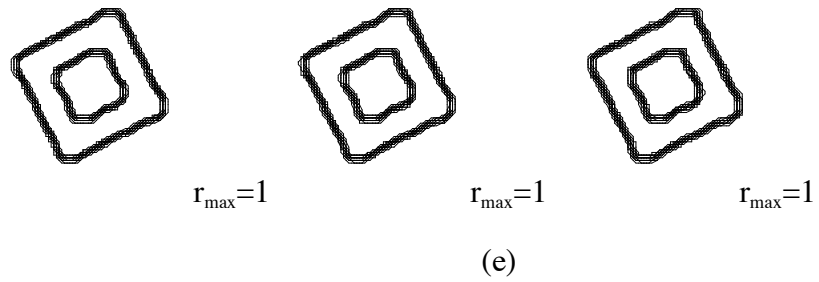
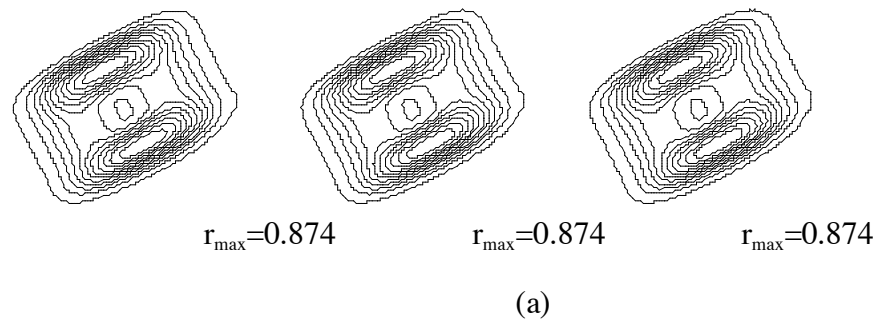


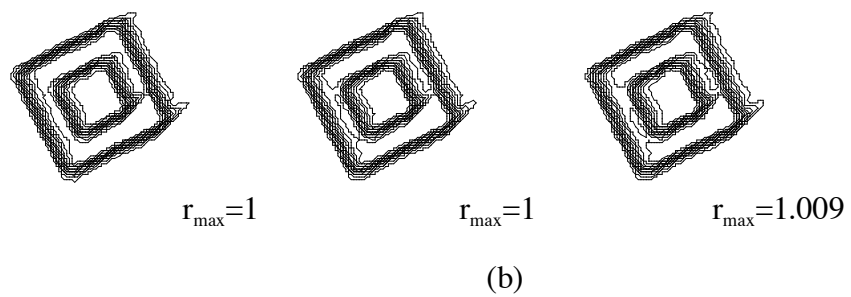
Fig. 13  $r$ -contour plots for the advection in an oblique flow field of the rotated hollow square problem over a structured grid.

low Co                      medium Co                      high Co

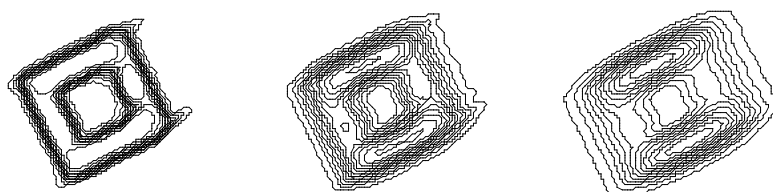
UPWIND



SMART



CICSAM



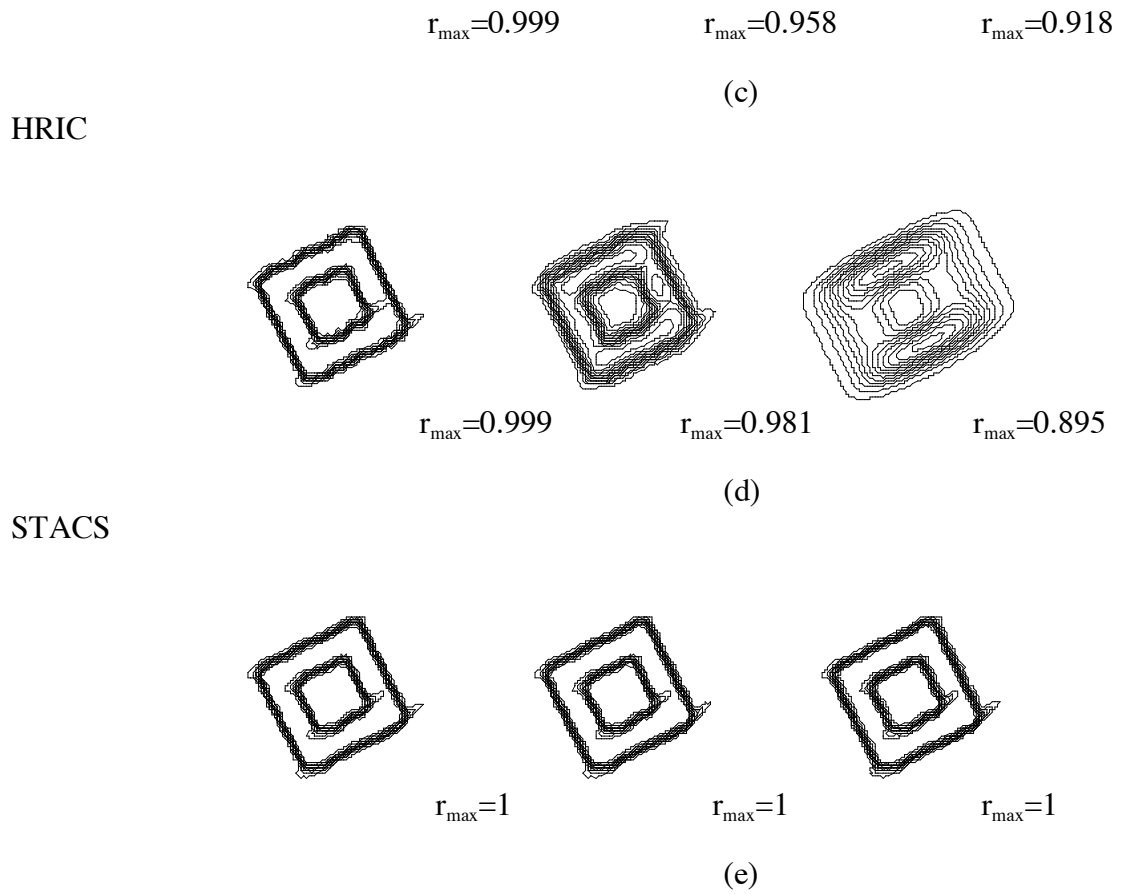


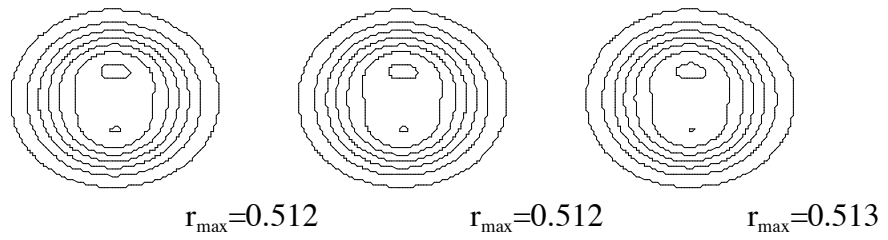
Fig. 14  $r$ -contour plots for the advection in an oblique flow field of the rotated hollow square problem over an unstructured grid.

low Co

medium Co

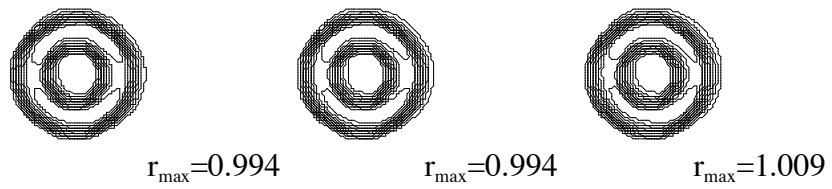
high Co

UPWIND



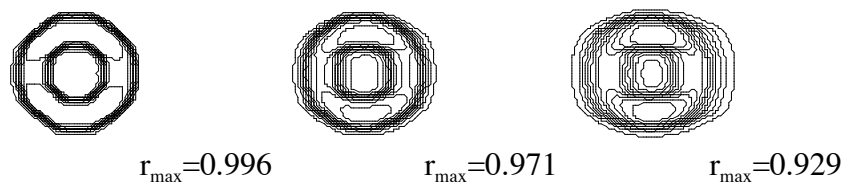
(a)

SMART



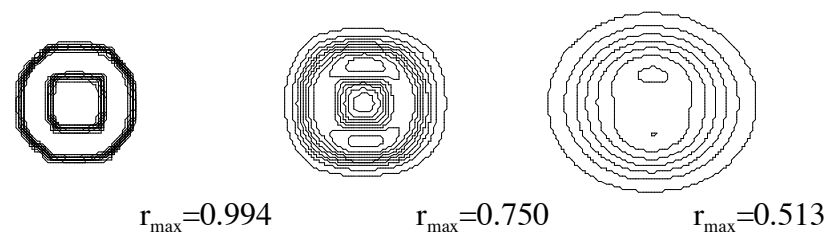
(b)

CICSAM



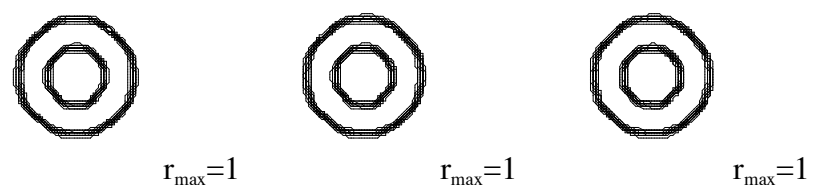
(c)

HRIC



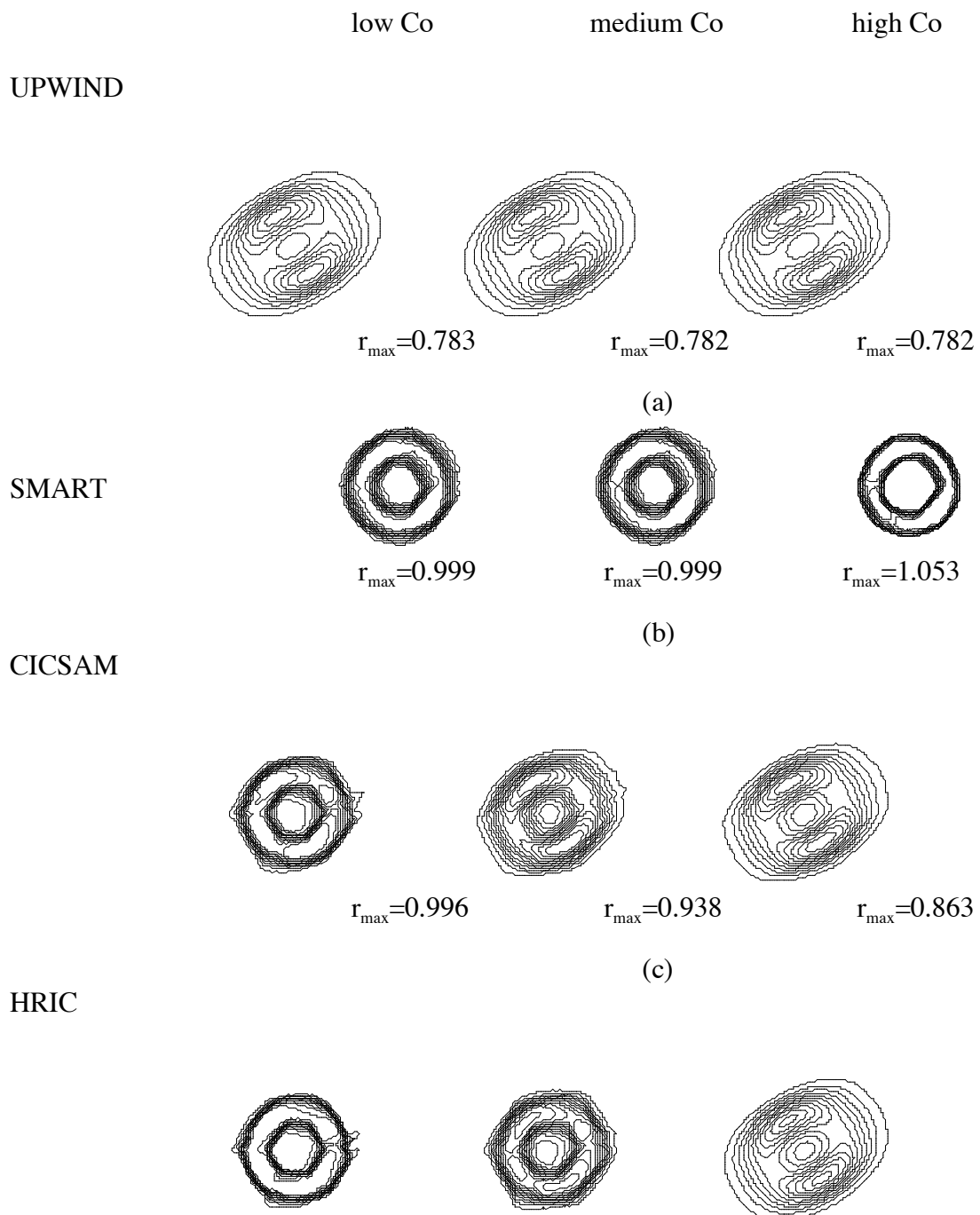
(d)

STACS



(e)

Fig. 15  $r$ -contour plots for the advection in an oblique flow field of the hollow circle problem over a structured grid.



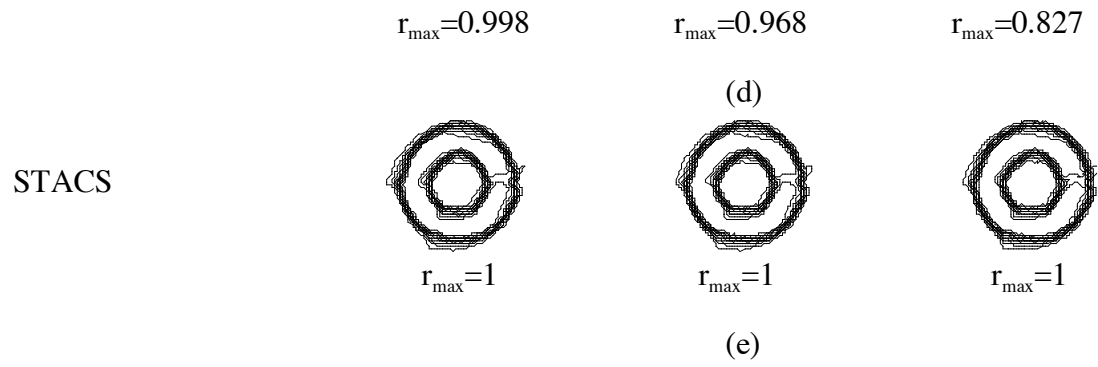
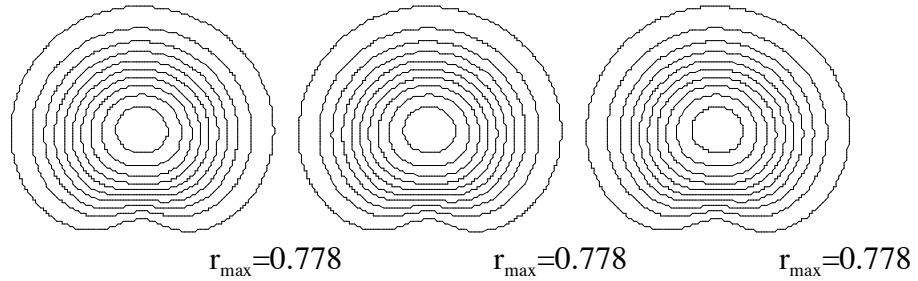


Fig. 16  $r$ -contour plots for the advection in an oblique flow field of the hollow circle problem over an unstructured grid.

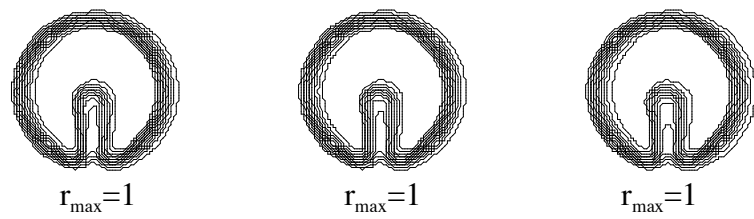
low Co                      medium Co                      high Co

UPWIND



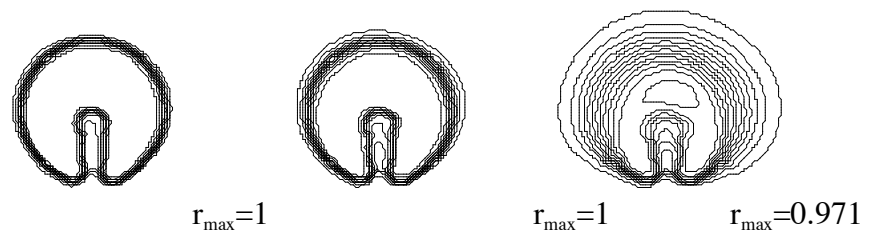
(a)

SMART



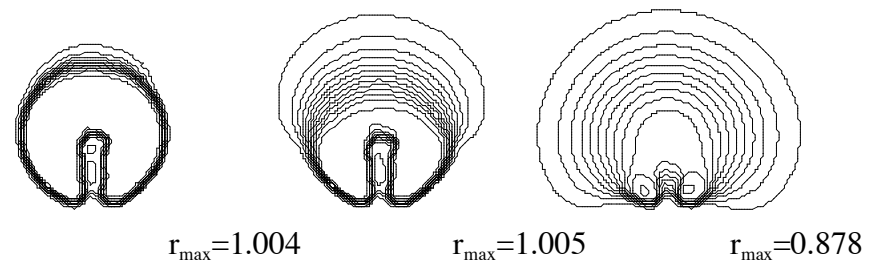
(b)

CICSAM



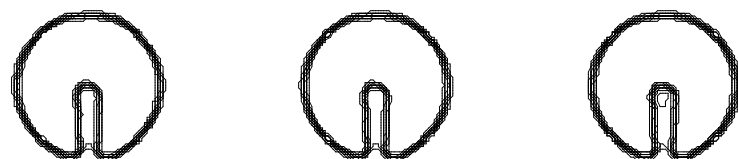
(c)

HRIC



(d)

STACS



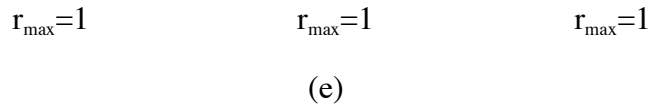
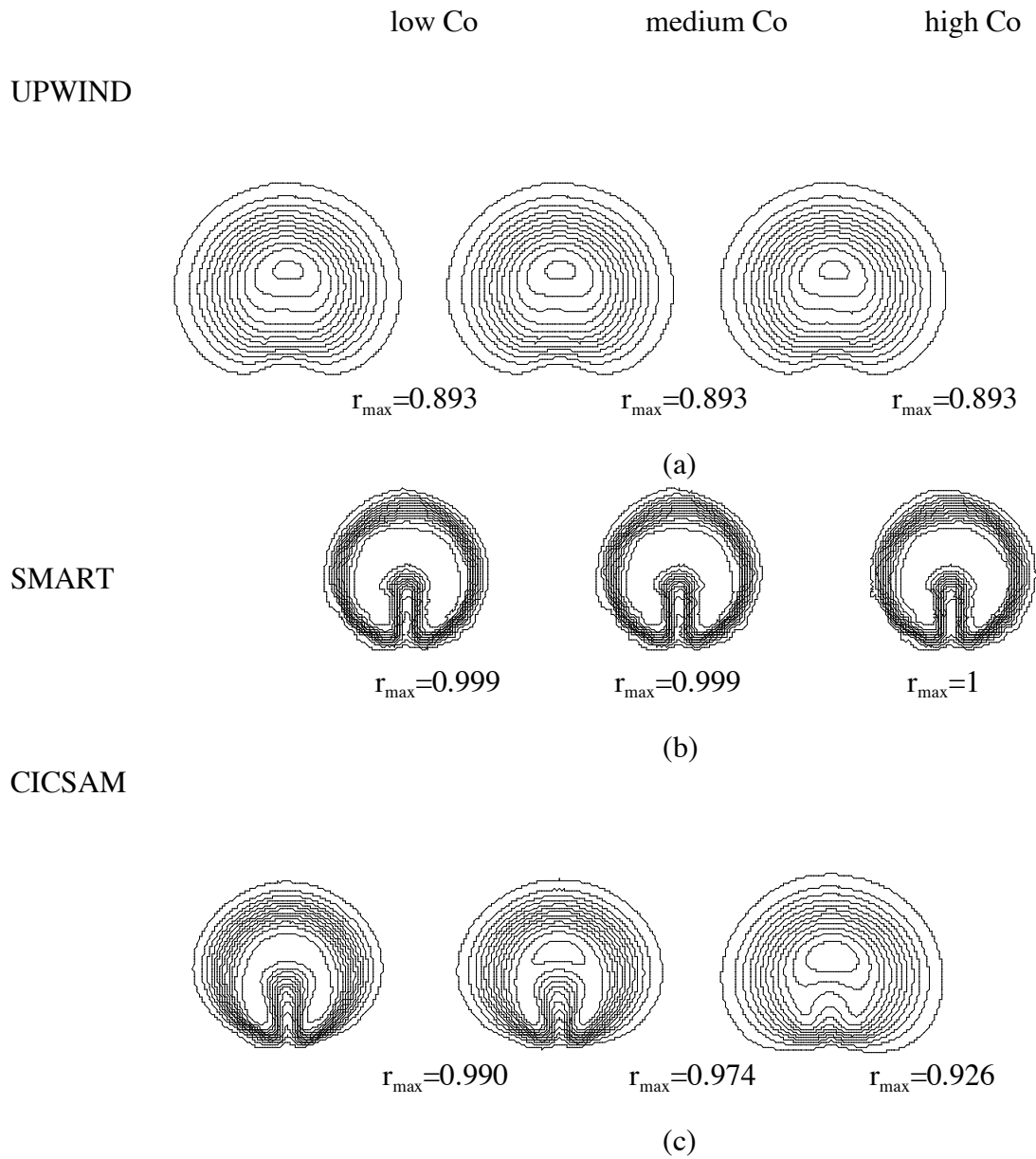
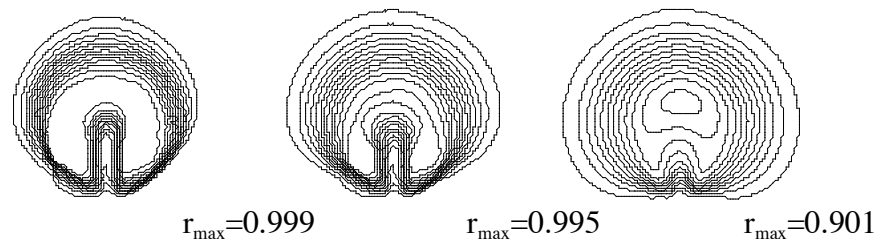


Fig. 17  $r$ -contour plots for the advection in a rotational flow field of the slotted circle problem over a structured grid.

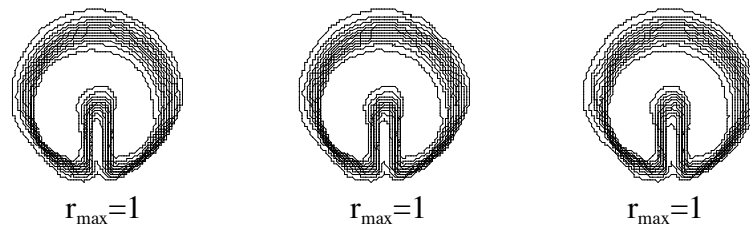


HRIC



(d)

STACS



(e)

Fig. 18  $r$ -contour plots for the advection in a rotational flow field of the slotted circle problem over an unstructured grid.



## References

---

- 1 Darwish, M. and Moukalled, F.,” An exact r-Factor TVD Formulation for Unstructured Grids,” IASTED International Conference on Applied Simulation and Modeling, Crete, Greece, June 25-28, 2002.
- 2 Darwish, M. and Moukalled, F.,” TVD Schemes for Unstructured Grids,” International Journal of Heat and Mass Transfer, vol. 46, no. 4, pp. 599-611, 2003.
- 3 Darwish, M. and Moukalled, F.,“ B-Express: A new Bounded Extrema Preserving Algorithm Strategy for Convective Schemes”, Numerical Heat Transfer, Part B: Fundamentals, vol. 37, no. 2, pp 227-246, 2000.
- 4 Darwish, M. and Moukalled, F.,” An Efficient Very High-Resolution Scheme Based on an Adaptive-Scheme Strategy”, Numerical Heat Transfer, Part B, vol. 34, pp. 191-213, 1998.
- 5 Darwish, M. and Moukalled, F., “A New Route for Building Bounded Skew-Upwind Schemes”, Computer Methods in Applied Mechanics and Engineering, vol. 129, pp. 221-233, 1996.
- 6 Moukalled, F. and Darwish, M.,”A High-Resolution Pressure-Based Algorithm for Fluid Flow at All Speeds”, Journal of Computational Physics, vol. 168, no.1, pp. 101-133, 2001.
- 7 Moukalled, F. and Darwish, M.,“A Unified Formulation of the Segregated Class of Algorithms for Fluid Flow at All Speeds,” Numerical Heat Transfer, Part B: Fundamentals, vol. 37, no. 1, pp 103-139, 2000.

- 
- 8 Darwish, M., Moukalled, F., and Sekar, B. "A Unified Formulation of the Segregated Class of Algorithms for Multi-Fluid Flow at All Speeds," 36<sup>th</sup> AIAA/ASME/SAE/ASEE Joint Propulsion Conference, Huntsville, Alabama, 16-19 July, 2000.
  - 9 Darwish, M., Moukalled, F., and Sekar, B. "A Unified Formulation for the Segregated Class of Algorithms for Multi-Fluid Algorithm at All Speeds," Numerical Heat Transfer, Part B: Fundamentals, vol.40, no. 2, pp. 99-137, 2001
  - 10 Shyy, W. and Chen, M.H., "Pressure-Based Multigrid Algorithm for Flow at All Speeds," AIAA Journal, vol. 30, no. 11, pp. 2660-2669, 1992.
  - 11 Brandt, A., "Multi-Level Adaptive Solutions to Boundary-Value Problems," Math. Comp., vol. 31, pp. 333-390, 1977.
  - 12 Rhie, C.M., "A Pressure Based Navier-Stokes Solver Using the Multigrid Method," AIAA paper 86-0207, 1986.
  - 13 Shyy, W. and Braaten, M.E., "Adaptive Grid Computation for Inviscid Compressible Flows Using a Pressure Correction Method," AIAA Paper 88-3566-CP, 1988.
  - 14 Darwish, M., Moukalled, F., and Sekar, B., "A Robust Multi-Grid Algorithm for Multifluid Flow at All Speeds," International Journal for Numerical Methods in Fluids, vol. 41, pp. 1221-1251, 2003.
  - 15 Ha, J., Cleary, P.W., Alguine, V., and Nguyen, T., "Simulation of die filling in gravity die casting using SPH and MAGMA soft", Proceedings of the Second International Conference on CFD in the Minerals and Process Industries Melbourne, 1999.

- 
- 16 Cleary, P.W. and Ha, J., "Three-dimensional modeling of high pressure die casting," *Journal of Cast Metals Research*, vol.12, pp. 357-365, 2000.
  - 17 Nichols, B.D., Hirt, C.W., and Hotchkiss, R.S.," SOLA-VOF: a solution algorithm for transient fluid flow with multiple free boundaries," Technical Report LA-8355, Los Alamos Scientific Laboratory, 1980.
  - 18 Nichols, B.D. and Hirt, C.W.," Methods for Calculating Multi-Dimensional, Transient Free-Surface Flows Past Bodies," *Proceedings of First International Conference of Numerical Ship Hydrodynamics*, Gaithersburg, ML, Oct. 20-23, 1975.
  - 19 Hirt, C.W. and Nichols, B.D., "Volume of Fluid (VOF) Method for the Dynamics of Free Boundaries," *J. Comp. Physics*, vol. 39, pp. 201, 1981.
  - 20 Leonard, B.P. and Mokhtari, S.," Beyond First-Order Upwinding: The Ultra-Sharp Alternative for Non-Oscillatory Steady-State Simulation of Convection," *International Journal for Numerical Methods in Engineering*, vol. 30, pp.729-766, 1990.
  - 21 Youngs, D.L.," An interface tracking method for a 3D Eulerian hydrodynamics code", Technical Report 44/92/35, Atomic Weapons Research Establishment, 1984.
  - 22 Puckett, E.G.," A volume of fluid interface tracking algorithm with applications to computing shock wave rarefaction," *Proceedings of the Fourth International Symposium on Computational Fluid Dynamics*, University of California at Davis, CA, 9-12 September, pp. 933-938, 1991.

- 
- 23 Unverdi, S.O. and Tryggvason, G., “ A front tracking method for viscous, incompressible multi-fluid flow”, *Journal of Computational Physics*, vol. 100, pp. 25-37, 1992.
  - 24 Noh, W.F. and Woodward, P., “SLIC (Simple Line Interface Calculations)”, *Lecture Notes in Physics*, Vol. 59, pp. 330-340, 1976.
  - 25 Rudman, M., “ Volume tracking methods for interfacial flow calculations”, *International Journal for Numerical Methods in Fluids*, vol. 24, pp. 671-691, 1997.
  - 26 Renardy, Y. and Renardy M., “PROST: Parabolic Reconstruction of Surface Tension for the volume-of-fluid Method”, *Journal of Computational Physics*, vol.183, No. 2, pp. 400-421, 2002.
  - 27 Harvie D.J.E, Fletcher D.F., “A new Volume of fluid advection algorithm: the defined donating region scheme”, *Int. J. Num. Methods Fluids*, vol. 38, p. 151-172, 2001
  - 28 Harlow, F.H. and Amsden, A.A., *Fluid dynamics*. Los Alamos National Laboratory report LA-4700, 1971.
  - 29 Lafaurie, B., Nardone, C., Scardovelli, R., Zaleski, S., and Zanetti, G.,” Modelling merging and fragmentation in multiphase flows with SURFER,” *Journal of Computational Physics*, vol. 113, pp. 134-147, 1994.
  - 30 Maronnier, V., Picasso, M., and Rappaz, J.,” Numerical Simulation of Free Surface Flows,” *Journal of Computational Physics*, vol. 155, pp. 439-455, 1999.
  - 31 Kothe, D.B., Williams, M.W., Lam, K.L., Korzekwa, D.R., Tubesing, P.K., and Puckett, E.G.,” A Second-Order accurate , Linearity preserving volume tracking

- 
- Algorithm for Free-Surface flows on 3-D unstructured meshes,” Proceedings of the 3<sup>rd</sup> ASME, JSME Joint Fluids Engineering Conference, San Francisco, California, USA, July 18-22, 1999.
- 32 Brackbill, J.U., Kothe, D.B., and Zemach, C.,“ A Continuum Method for Modelling Surface Tension,” *Journal of Computational Physics*, vol. 100, pp. 335-354, 1992.
- 33 Kothe, D.B., and Mjolsness, R.C.,” RIPPLE: A new model for incompressible flows with free Surfaces,” *AIAA Journal* , vol 30, no. 11, pp 2694-2700, 1992.
- 34 Ubbink, O. and Issa, R.,“ A Method for Capturing Sharp Fluid Interfaces on Arbitrary Meshes”, *Journal of Computational Physics*, vol. 153, pp. 26-50, 1999.
- 35 Moukalled F., Darwish M.S.," A New Bounded-Skew Central Difference Scheme- part I: Formulation & Testing,” *Numerical Heat Transfer, Part B: Fundamentals*, vol. 31, pp. 91-110, 1996.
- 36 Muzaferija S., and Peric M.,” Computation of free-surface flows using interface-tracking and interface-capturing methods,” in Mahrenholtz O, Markiewicz M. (eds.), *Nonlinear Water Wave Interaction*, Computational Mechanics Publications, Southampton, 1998.
- 37 Rider, W.J. and Kothe, D.B.,“ Stretching and Tearing Interface Tracking Methods,” *AIAA Paper 95-1717*, Presented at the 12th AIAA CFD Conference, San Diego, June 19-22, LANL Report LA-UR-95-1145, 1995.
- 38 Rider, W.J. and Kothe, D.B.,” Reconstructing Volume Tracking,” *Journal of Computational Physics*, vol. 141, pp. 112-152, 1998.

- 
- 39 Leonard B.P., "The ULTIMATE Conservative Difference Scheme Applied to Unsteady One-Dimensional Advection," *Computer Methods in Applied Mechanics and Engineering*, vol. 88, pp. 17-74, 1991.
- 40 Ramshaw, J.D. and Trapp, J.A., "Numerical Technique For Low Speed Homogeneous Two Phase Flow with a Sharp Interface", *J. Computational Physics*, vol. 21, pp. 438, 1976.
- 41 Muzaferija, S., Peric, M., Sames, P., and Schellin, P., "A Two-Fluid Navier-Stokes solver to Simulate Water Entry," *Proceedings of the Twenty-Second Symposium on Naval Hydrodynamics*, pp.638-649, 1998.
- 42 Leonard, B.P. and Niknafs, H.S., "Sharp monotonic resolution of discontinuities without clipping of narrow extrema," *Computers and Fluids*, vol. 19, no. 1, pp. 141-154, 1991.
- 43 Leonard, B.P., "Stable and accurate convective modeling procedure based on quadratic upstream interpolation," *Computer Methods in Applied Mechanics and Engineering*, pp. 59-98, 1990.
- 44 Jasak, H., "Error Analysis and Estimation for the Finite Volume Method With Applications to Fluid Flows," Ph.D Thesis, Department of Mechanical Engineering, Imperial College of Science, Technology and Medicine, June 1996.
- 45 Darwish, M., "A New High-Resolution Scheme Based on the Normalized Variable Formulation," *Numerical Heat Transfer, part B*, vol. 24, pp. 353-373, 1993.

- 
- 46 Osher, S. and Chakravarthy, S.,” Upwind schemes and boundary conditions with applications to Euler equations in general geometries,” *Journal of Computational Physics*, vol. 50, pp. 447–481, 1983.
  - 47 Rudman, M.,” Volume-Tracking Methods for Interfacial Flow Calculations,” *International Journal for Numerical Methods in Fluids*, vol. 24, pp. 671-691, 1997.
  - 48 Zalesak, S.T.,” Fully Multi-Dimensional Flux Corrected Transport Algorithms for Fluid Flow,” *Journal of Computational Physics*, vol. 31, pp. 335-362, 1979.